DOI: 10.13009/EUCASS2023-421
Aerospace Europe Conference 2023 – 10TH EUCASS – 9TH CEAS

Aerodynamic simulation of the near field of an aircraft using different mesh adaptation strategies

Younes Bouhafid⋆ †, *Nicolas Bonne*⋆† *and Laurent Jacquin*⋆
⋆*ONERA/DMPE*
Palaiseau F-91123 - France
younes.bouhafid@onera.fr · nicolas.bonne@onera.fr
†Corresponding author

Abstract

The formation of condensation trails (contrails) from aircraft emissions at high altitudes and their subsequent evolution can have a significant impact on climate. Understanding the evolution of contrails in the near field of an aircraft requires simulations that accurately solve the microphysics of ice formation, dilution due to jet dynamics, and rolling-up of the plume around the wing-tip vortices pair. Anisotropic mesh adaptation techniques can be used to better resolve regions of high flow gradients such as wing-tip vortices, shear layers, vorticity sheets and shock waves, enabling more accurate predictions of the formation and evolution of contrails and their impact on the atmosphere and climate. This paper presents a comparison of three different mesh adaptation strategies based on different sensors. Simulations of the near field of the Common Research Model configuration with jet engines during cruise flight are carried out for each sensor. Their accuracy is evaluated by predicting the wing-tip vortex circulation, lift, and drag coefficients of the aircraft and thermodynamic quantities inside the engine jet. The results obtained clearly demonstrate the potential of mesh adaptation for RANS simulations of the flow field in the near field of an airliner up to twenty wingspans behind the wing.

1. Introduction

Condensation trails, also known as contrails, are ice crystals clouds that are formed by aircraft emissions at flight altitudes. Their formation and evolution can have a significant impact on the atmosphere and climate as shown by a recent compilation of studies [6] of the effects of aviation's climate forcing. In order to develop strategies to reduce their undesirable impacts, the investigation of contrail formation near the aircraft is necessary as long-term effects of the early dynamic in the near-field were observed [17].

The early stage of a contrail's life, that is to say the first seconds, is dominated by the ice formation microphysics, the dilution due to the jet dynamic, and the rolling-up of the jet plume around the wing-tip vortices. Thus, in order to better understand contrail evolution in the near field of an aircraft, it is important to carry out simulations that accurately solve these processes. However, if the computation mesh is too coarse, the contrail microphysics and chemistry will be poorly resolved and numerical diffusion will cause the dissipation of the vortices, resulting in vortex strength weakening. This can lead to an inaccurate prediction of the contrail evolution. Indeed, underestimating the vortex strength will lead to an underestimation of the plume mixing around wing-tip vortices and the descent velocity of the vortex pair carrying the ice crystals. More precisely, the wing-tip vortices carry the ice crystals downwards through vortex mutual induction, which results in adiabatic heating of these ice crystals inside the vortex pair, and potentially to ice crystals loss [16] due to ambient temperature increase. Moreover, as the vortex pair continues moving downward, interactions between the vorticity field of the vortices pair and atmospheric stratification result in the creation of a secondary wake [17, 12] which can carry ice crystals back to the flight altitude. As a consequence, the role of the vortex pair in the formation of persistent contrails is critical. Therefore, if a prior CFD (Computational Fluid Dynamics) simulation of the near field of an aircraft is to be used to initialize the wake vortices descent regime, it is then crucial to address these issues with high-fidelity computations.

A possible solution lies in the use of anisotropic mesh adaptation techniques. Such techniques can be employed to better resolve important regions for the contrail dynamic, such as those near the aircraft engine exhaust where ice crystals form, as well as regions of wing-tip vortices. Moreover, anisotropic mesh adaptation has several advantages compared to classical mesh convergence studies with handcrafted meshes. For example, mesh convergence is reached faster [1] and only the physically relevant parts of the flow are finely meshed, resulting in diminishing the CPU cost

DOI: 10.13009/EUCASS2023-421

of the computation. Practically speaking, anisotropic mesh adaptation allows automation of the often time-consuming mesh generation step, and it lowers the time that must be spent to generate a satisfying mesh in the CFD pipeline.

Anisotropic mesh adaptation has been successively used for RANS simulations. As an example, Balan [2] performed anisotropic mesh adaptation for the aerodynamic flow field over the ONERA M6 wing based on the Mach number interpolation error. It is shown that for computations based on adapted meshes, forces, and pitching moment converge faster towards the values obtained with a fine fixed mesh compared to handcrafted fixed meshes. Anisotropic mesh adaptation has also been used on more complex geometry. Alauzet [1] demonstrated the ability of anisotropic mesh adaptation to accurately capture aerodynamic phenomena for the NASA HL-CRM (High Lift Common Research Model) geometry representative of a B777 on high-lift configuration [14]. Finally, anisotropic mesh adaptation was used by Montreuil [11] for a RANS numerical simulation of contrails in the near field of the CRM geometry for which engines ejecting exhaust gases were added.

However, since mesh adaptation is based on an optimization process, the obtained mesh will depend on the optimized physical variable. Therefore, it is significant to compare the influence of the physical variable used for the mesh adaptation process and discuss which one is best suited for contrail simulations in an aircraft near field. This is the objective of this work.

This paper is organized as follows. Section II provides a brief summary of the theoretical framework of anisotropic mesh adaptation. Section III presents a description of the numerical setup, and finally, the results are discussed in section IV.

2. Anisotropic mesh adaptation framework

Metric-based anisotropic mesh adaptation is a powerful technique that allows for the efficient and accurate simulation of fluid flows by adjusting the mesh resolution and orientation based on the local solution error and the underlying physics. The basic idea behind anisotropic mesh adaptation is to refine the mesh in areas where the solution is changing rapidly or where the physics is highly anisotropic, while coarsening the mesh in regions with smoother or isotropic behavior.

The mesh adaptation software used in this work is Feflo.a from INRIA. It is based on the notions of metric tensor, Riemannian metric space and so-called continuous mesh theory. A thorough description of such theory can be found in Loseille and Alauzet's work [7, 8]. A short description of the key ideas of metric-based anisotropic mesh adaptation is given in this section.

2.1 Riemaniann metric space and continuous mesh

Let $\mathcal{M}(\mathbf{x})$ be a metric tensor field that varies smoothly on a domain Ω of $\mathbb{R}^3$. Such tensor allows to define concepts of length and orientation in what is called a Riemannian metric space. This space is referred as $\mathbf{M} = \mathcal{M}(\mathbf{x})_{x\in\Omega}$. The length of an edge $\mathbf{ab}$ in such space is defined by:

$$\ell_{\mathcal{M}}(\mathbf{ab}) = \int_0^1 \sqrt{{}^t\mathbf{ab}\mathcal{M}(\mathbf{a} + t\mathbf{ab})\mathbf{ab}}\, \mathrm{d}t \tag{1}$$

Orientation and anisotropy are prescribed by the eigenvectors and eigenvalues of $\mathcal{M}(\mathbf{x})$ since $\mathcal{M}(\mathbf{x})$ is a symmetric positive definite tensor.

Riemannian metric spaces form the basis of the continuous mesh concept. Let K be a tetrahedron in Ω. K is said to be unit with respect to $\mathcal{M}$ if the length of its edges is equal to one in the metric $\mathcal{M}$, that is to say $\ell_{\mathcal{M}}(\mathbf{e}_i) = 1$. It can be shown [7] that for a given metric $\mathcal{M}$, there exists an infinity of elements K that are unit with respect to $\mathcal{M}$. Moreover, for a given K, it can be shown that there exists a unique $\mathcal{M}$ for which K is unit with respect to $\mathcal{M}$. Thus, we can define the class of equivalence *with respect to* $\mathcal{M}$ in the set of tetrahedron elements.

2.2 Discrete mesh/continuous mesh duality

In that sense, a duality between the continuous entity $\mathcal{M}$ and the discrete entity K can be derived. Indeed, it is possible to rewrite $\mathcal{M}(\mathbf{x})$ using orthogonal eigendecomposition as:

$$\mathcal{M}(\mathbf{x}) = d^{\frac{2}{3}}(\mathbf{x})\mathcal{R}(\mathbf{x})diag(r_1^{-\frac{2}{3}}, r_2^{-\frac{2}{3}}, r_3^{-\frac{2}{3}})^t\mathcal{R}(\mathbf{x}) \tag{2}$$

DOI: 10.13009/EUCASS2023-421

where the density d is defined by $d = (h_1h_2h_3)^{-1} = (\lambda_1\lambda_2\lambda_3)^{-\frac{1}{2}}$ with $h_i = \lambda_i^{\frac{1}{2}}$, λ_i being the eigenvalues of $\mathcal{M}$, and the anisotropic quotients r_i by $r_i = h_i^3(h_1h_2h_3)^{-1}$. The complexity C of the metric space $\mathbf{M}$ is defined by:

$$C(\mathbf{M}) = \int_\Omega d(\mathbf{x})d\mathbf{x} = \int_\Omega \sqrt{\det(\mathcal{M}(\mathbf{x}))}d\mathbf{x} \tag{3}$$

The duality between continuous and discrete elements is as follows: complexity C is analogous to the number of vertices in a discrete tetrahedral mesh, the orthogonal matrix $\mathbf{R}$ is analogous to the orientation of element K and r_i is similar to the stretching of element K. In practice, asking that all the elements K of a discrete mesh to be unit with respect to $\mathbf{M}$ is too big of a constraint. This can be solved by relaxing the constraint on edge lengths and asking the volume of K to be superior to a certain value that depends on its edge lengths. K is then said to be quasi-unit with respect to $\mathcal{M}(\mathbf{x})$. A mesh $\mathcal{H}$ composed of tetrahedral elements K is then said to be unit with respect to a Riemannian metric space $(\mathcal{M}(\mathbf{x}))_{\mathbf{x}\in\Omega}$ if all its elements are quasi-unit.
The duality can also be expressed with respect to the computation of a linear interpolation error. Indeed, given a smooth function u and u_Q its quadratic approximation around a point $\mathbf{a}$, there exist a unique function $\pi_\mathcal{M}$ such that for a certain norm [7]:

$$\forall \mathbf{a} \in \Omega, \quad |u - \pi_\mathcal{M} u|(\mathbf{a}) = 2\frac{\left\|u_Q - \Pi_h u_Q\right\|_{\mathbf{L}^1(K)}}{|K|} \tag{4}$$

for every K unit element with respect to $\mathcal{M}(\mathbf{a})$ and where Π_h is the linear interpolation operator. $\| \|_{\mathbf{L}^1(K)}$ refers to the L^1 integration inside the element K. From now on, $\mathbf{M}$ will be referred as *continuous mesh*. Eq.4 allows for the computation of a local error. We define the global interpolation error for both the discrete unit mesh $\mathcal{H}$ and the continuous mesh $\mathbf{M}$ by:

$$\|u - \Pi_h u\|_{\mathbf{L}^1(\Omega_h)} = \sum_{K\in\mathcal{H}} \|u - \Pi_h u\|_{\mathbf{L}^1(K)} \tag{5}$$

$$\|u - \pi_\mathcal{M} u\|_{\mathbf{L}^1(\Omega)} = \int_\Omega |u - \pi_\mathcal{M} u|(\mathbf{x})d\mathbf{x} \tag{6}$$

Loseille [7] showed numerically that those two quantities are strongly correlated. Thus, decreasing the continuous linear interpolation error will decrease the discrete linear interpolation error.

2.3 Application to CFD mesh adaptation

The goal of mesh adaptation is to find a certain mesh $\mathcal{H}$ that minimizes the approximation error between the exact solution and the numerical solution for a given number of nodes N. This is a combinatorial problem that is in practice impossible to solve. The idea then is to reformulate this problem in the frame of continuous mesh and construct a unit discrete mesh when the continuous solution is known. First, given certain assumptions [8], it is possible to derive an inequality relation between the linear interpolation error and the approximation error. Let R_h be a reconstruction operator respecting such assumptions and applied to the numerical approximation u_h of a function u. There exist α with $0 \leq \alpha < 1$ such that [8]:

$$\|u - u_h\| \leq \frac{1}{1-\alpha}\|R_h u_h - \Pi_h R_h u_h\| \tag{7}$$

Thus, it possible to control the approximation error by controlling the linear interpolation error of the reconstructed function $R_h u_h$. In practice, the reconstruction operator R_h is built using P2-Lagrange test functions and L^2 projection. The minimization problem of the continuous linear interpolation error can be written:

$$\text{Find } \mathbf{M}_{\mathbf{L^p}} = \min_{\mathbf{M}} \left(\int_\Omega (R_h u_h - \pi_\mathcal{M}(R_h u_h))^p\right)^{\frac{1}{p}} \tag{8}$$

with the constraint:

$$C(\mathbf{M}) = \int_\Omega d = \mathcal{N} \tag{9}$$

The error is computed using the L^p norm. This problem is solved using calculus of variations and the unique solution is [7]:

$$\begin{aligned} \mathcal{M}_{L^p} &= \det(|H_{R_h u_h}|)^{\frac{-1}{2p+3}} |H_{R_h u_h}| D \\ D &= N^{\frac{2}{3}} \left(\int_\Omega \det(|H_{R_h u_h}|)^{\frac{p}{2p+3}}\right)^{-\frac{2}{3}} \end{aligned} \tag{10}$$

DOI: 10.13009/EUCASS2023-421

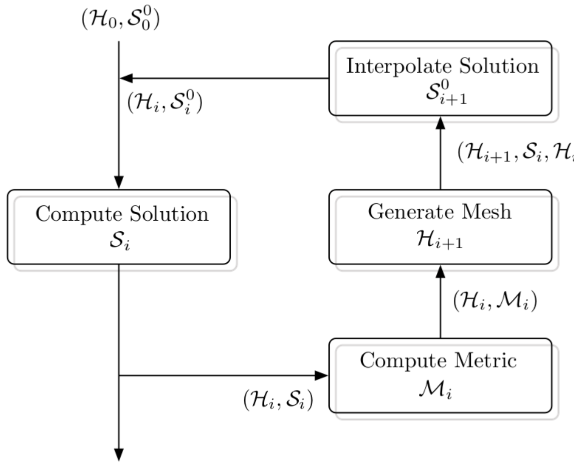

Figure 1: Mesh adaptation algorithm [9]

where $H_{R_h u_h}$ is the Hessian matrix of the reconstructed function containing all the information about the anisotropy and curvature of the reconstructed flow field. Knowing the continuous mesh, it is possible to reconstruct a discrete mesh that is unit with respect to the continuous mesh. Anisotropic mesh adaptation being a non-linear it problem, it is solved through an iterative process.

For a RANS simulation, the first step is to converge the solution on an initial coarse mesh $\mathcal{H}_0$. Then, for a given complexity N, the mesh is adapted with respect to a physical variable u_h, called sensor in the context of mesh adaptation. The solution $\mathcal{S}_0$ is then interpolated on the new mesh $\mathcal{H}_1$ and is used as an initial condition. A new solution $\mathcal{S}_1$ is then computed. That process is repeated for the same complexity a certain number of times. The complexity N is then increased and the mesh is adapted again until the pair solution/mesh has converged. A description of the algorithm can be found in Fig.1.

3. Numerical setup

3.1 Geometry and domain

The geometry used in the simulations consists of the NASA Common Research Model aircraft for which engines, horizontal tail plane (HTP), and vertical tail plane (VTP) were added at ONERA. It is the same geometry used by Montreuil in his work [11] and it can be seen in Fig.2. The computational domain is a rectangular parallelepiped with dimensions Lx, Ly and Lz. Only half of the airplane is taken into account as the flow is supposed to be symmetrical with respect to the (x,z) plane. This eliminates the need to model the entire aircraft geometry in the simulation. The size of the domain downstream of the plane is about twenty wingspans. The domain size and different length scales are summarized in Table 1.

Dimension	Size
Wingpsan b	58.76 m
Wing area S	383 m^2
Mean chord c_m	6.5 m
L_x	$[-10b : 20b]$
L_y	$[0 : 10b]$
L_z	$[-10b : 10b]$

Table 1: Dimensions of the computational domain

DOI: 10.13009/EUCASS2023-421

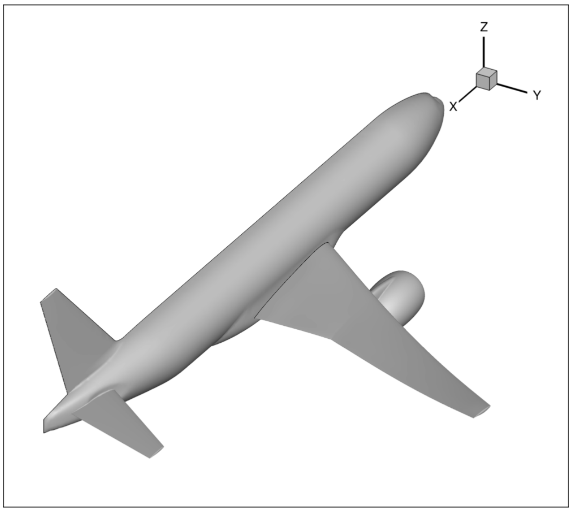

Figure 2: CRM wing/body/engine geometry used in the simulations

Location	**Boundary condition**
x=-10b	Inlet
x=20b	Oulet
y=0	Symmetry
y=10b	Outlet
z=-10b	Inlet
z=10b	Outlet

Table 2: Boundary conditions

3.2 Computational setup, boundary and initial conditions

Typical cruise flight conditions at an altitude of 10 km are used. Flight Mach number M is $M = 0.85$ and the angle of attack is $\alpha = 3°$. The engine inlet seen in Fig.3 is modeled as a subsonic outlet with imposed static pressure, while the engine primary outlet and secondary outlet seen in Fig.3 are modeled as subsonic inlets with given total pressure and total temperature values. The values were chosen in order to satisfy mass conservation between the inlet and the outlet. The engine was designed to be representative of an UHBR (Ultra High Bypass Ratio) engine with a bypass ratio of 12 [11]. The engine inlet models the action of the fan with a pressure ratio of 1.4. We apply a no-slip condition for all solid surfaces. The values used for the simulation are summarized in Table 3.

All the numerical simulations of this study were performed using ONERA's in-house compressible CFD solver CHARME from the multi-physics simulation platform CEDRE. Reynolds-averaged Navier-Stokes (RANS) equations

Atmospheric and Engine conditions				
Flight conditions	**Ma**	α	**P**	**T**
	0.85	3°	264.37 hPa	223.15 K
Core flow	**Total temperature**	**Total pressure**		
	626.41 K	530.01 hPa		
Secondary flow	297.23 K	699.21 hPa		
Engine inlet	**P**			
	370.118 hPa			

Table 3: Atmospheric and engine conditions

DOI: 10.13009/EUCASS2023-421

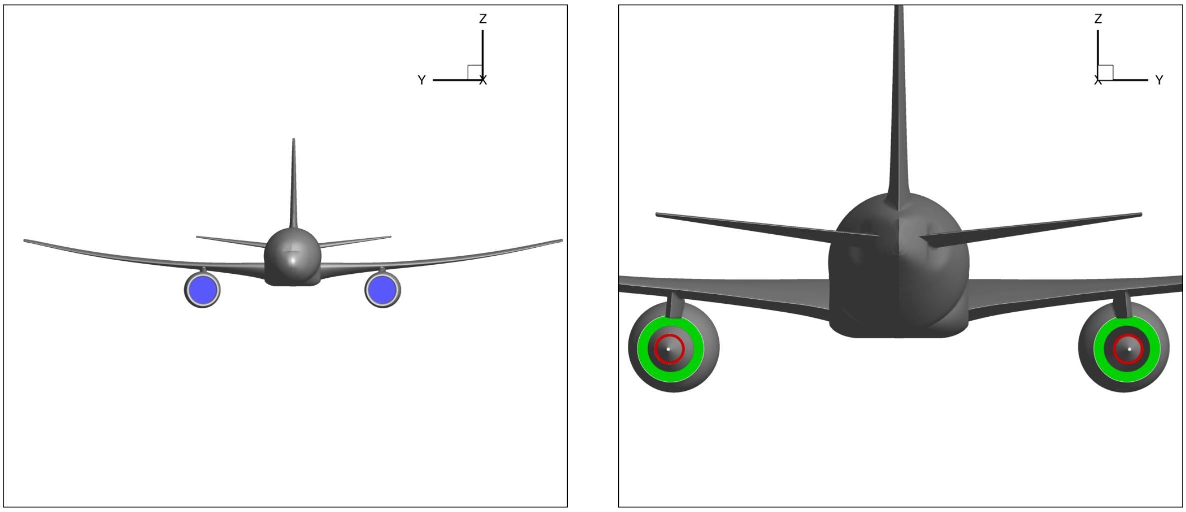

Figure 3: Close-up of the engine primary outlet (red), secondary outlet (green) and inlet (blue).

are solved using the finite volume method on an unstructured mesh. Only the aerodynamic field is computed. Chemistry and Ice formation microphysics is not taken into account in this work.

The RANS model used for the calculations is the DRSM (Differential Reynolds-stresses modeling) model developed in the European ATAAC project [15]. Such a model is known to be more accurate for swirling flows, like wing-tip vortices, compared to standard two-equations models such as k-ω or k-ϵ models. Indeed, RSM models solve an equation for each Reynolds stress and the Reynolds stress tensor is no longer required to be aligned with the mean strain-rate tensor. It has been shown [4] that because of the effects of curvature and rotation, those two tensors are misaligned inside a wing-tip vortex and thus the turbulent viscosity hypothesis used in two-equations model is no longer valid. The drawbacks of using DRSM model are its increased cost as more equations are solved and its numerical robustness compared to well-tested two-equations models. Temporal integration was performed using the implicit Euler scheme based on local time step constrained by the Courant number.

3.3 Mesh adaptation

Anisotropic mesh adaptation was carried out with INRIA's software Feflo.a. Four different meshes and three different sensor variables are considered in this work. A first mesh is adapted with respect to the crossflow velocity $CF = \sqrt{V_y^2 + V_z^2}$ where V_y and V_z are respectively the mean velocities along the y-direction and the z-direction in the ground reference frame. This was the sensor variable used by Montreuil in his work [11]. A second mesh is adapted with respect to total mean energy $TE = c_v T + \frac{1}{2}U^2$ where c_v is heat capacity at constant volume, T is static temperature and U is the mean velocity in the aircraft reference frame. A third mesh is adapted with respect to total kinetic energy $KEG = \frac{1}{2}V^2 + k$ where k is the mean kinetic turbulent energy obtained from the RANS simulations. Finally, a fourth mesh is adapted with respect to the KEG sensor variable but for which prism layers with $N = 10$ layers were added on the aircraft to resolve the boundary layer with a wall function and with y_+ values around 80.

Only the volume was adapted for all the meshes and the surface mesh was left untouched. The number of mesh cells for the different iterations of the mesh adaptation process is displayed in Fig.4. The interpolation error is computed with the L^4 norm for the first three meshes while the L^2 norm is used for the fourth mesh with prism layers. Indeed, the L^4 norm has been shown to provide a better meshing of the boundary layer compared to the L^2 norm whereas the L^2 norm has been shown to be more sensitive to the aircraft's wake [2]. As a consequence, if prism layers are used on solid surfaces, L^2 norm seems to be more appropriate. Four different complexities, defined in section II.B, are considered in the mesh adaptation loop:

$$C = \{25000, 50000, 100000, 200000\}$$

Complexity is analogous to the number of vertices inside a discrete mesh. For each complexity, three meshes are adapted, giving in total twelve meshes for each sensor plus the initial coarse mesh. At each step, the previous solution is interpolated on the new mesh to not restart the computation from the beginning. The residuals tend then to decrease a lot quicker. The parameters used for mesh adaptation are summarized in Table 4.

DOI: 10.13009/EUCASS2023-421

Mesh adaptation parameters	Sensor	L^p norm	Prism layers
Mesh A	CF	L^4	No
Mesh B	TE	L^4	No
Mesh C	KEG	L^4	No
Mesh D	KEG	L^2	Yes

Table 4: Mesh adaptation parameters

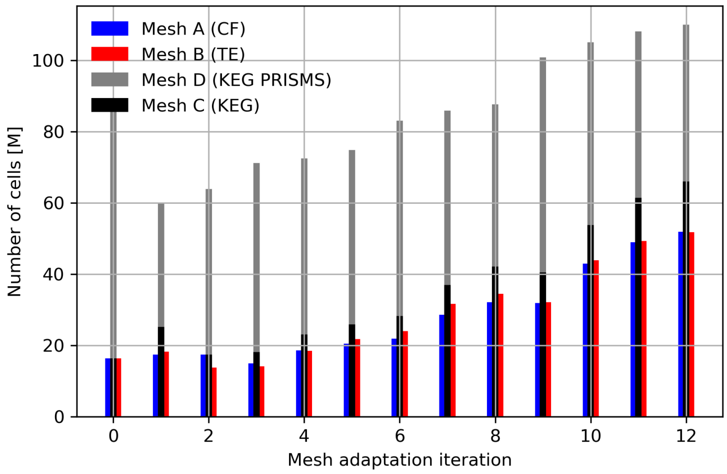

Figure 4: Number of cells in millions for the adapted meshes

4. Results and discussion

4.1 Wing-tip vortex dynamic

In this section, we analyze for each sensor variable the effect of mesh adaptation on the circulation Γ of the wing-tip vortex. The circulation is computed by integrating vorticty in a plane cut along the x-axis. Theoretical circulation is computed using the formula for elliptical loading:

$$\Gamma = \frac{C_L U_\infty S}{\pi b} \tag{11}$$

Circulation as a function of distance downstream of the aircraft is plotted in Fig.5a, Fig.5b, Fig.5c and Fig.5d for respectively mesh iteration n°3, 6, 9 and 12.

The lift coefficient C_L for the Common Research Model aircraft for the cruise flight conditions considered in this work was experimentally obtained by Rivers [13] through wind tunnel measurements. It is estimated to be between 0.46 and 0.53, experimental uncertainty being quite important. Knowing this value, theoretical circulation is then estimated to be between 487 m^2/s and 561 m^2/s. As we progress in the mesh adaptation loop, the value of the computed circulation gets closer for each sensor variable to the theoretical value. At iteration n°9, all the computed circulations fall within the range of theoretical values, except for the KEG mesh without the prism layers (mesh C). Moreover, the more the mesh is refined, the more the circulation remains constant with respect to distance. The mesh inside the vortex core gets more and more refined and the vortex strength is conserved throughout the computational domain as predicted by Kelvin's theorem. However, it seems that mesh D defined in Table 4 converges faster. Further analysis of mesh cuts showed that at the same complexity, mesh resolution inside the vortex core is higher compared to the three other meshes. This was already observed by Balan [2] where it was noticed that using L^2 norm made mesh adaptation more sensitive to the aircraft's wake comparatively to L^4 norm. On the other hand, L^4-norm adaptation is supposed to be more sensitive to the boundary layer on solid surfaces. This was not observed in this work as the y_+ values on the wing were observed to be too high for all mesh iterations, whether wall functions were used or not. The boundary layer was very poorly resolved on the wing for mesh A, B and C. One possible explanation is that forcing

DOI: 10.13009/EUCASS2023-421

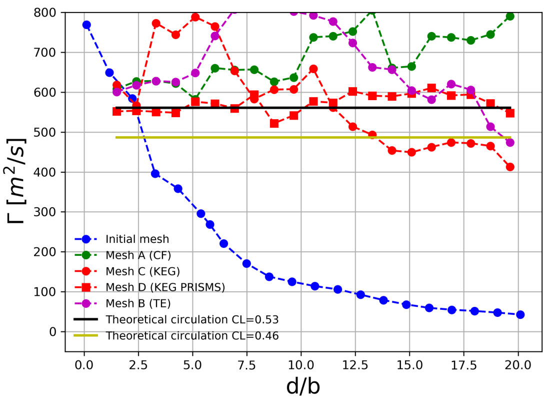

(a) Wing-tip vortex circulation as a function of distance for mesh iteration $n°3$

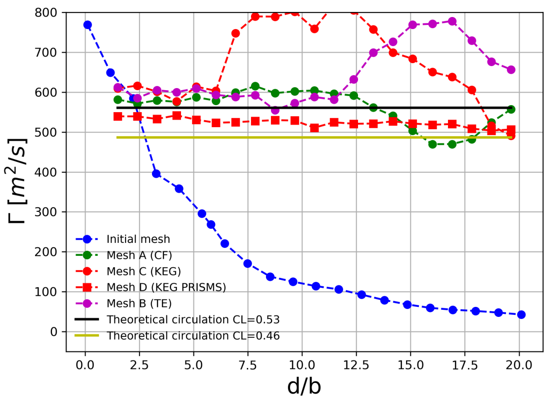

(b) Wing-tip vortex circulation as a function of distance for mesh iteration $n°6$

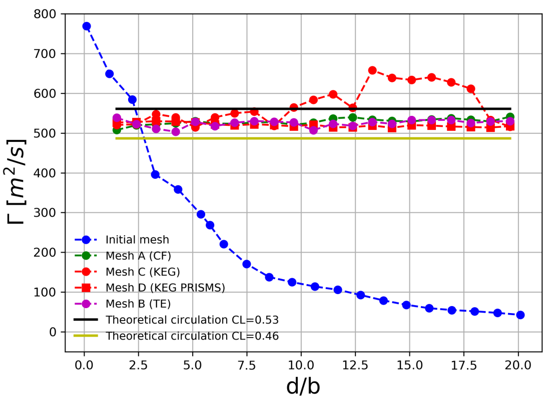

(c) Wing-tip vortex circulation as a function of distance for mesh iteration $n°9$

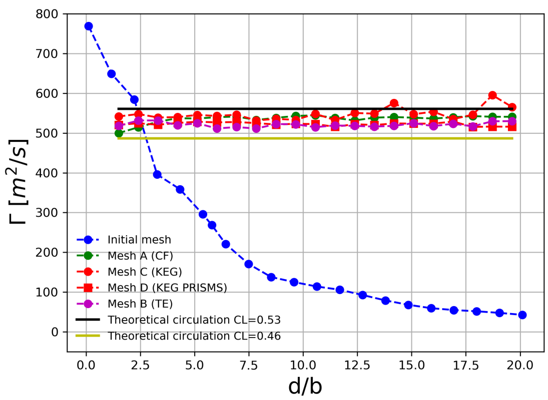

(d) Wing-tip vortex circulation as a function of distance for mesh iteration $n°12$

Figure 5: Wing-tip vortex circulation as a function of distance in wingspans for different mesh iterations

the mesh adaptation algorithm to leave the surfaces untouched was too great of a constraint for the boundary layer to be meshed correctly.

The lift coefficient C_L and the drag coefficient C_D obtained by numerical integration of the pressure and viscous forces on the aircraft surface are plotted in Fig.6 and Fig.7. From mesh iteration n°1 to mesh iteration n°6, no wall functions were used for mesh A, B and C. C_L and C_D were then respectively overestimated and underestimated compared to theoretical values. From mesh iteration n°7, wall functions were used and this resulted in decreasing the value of C_L and increasing the value of C_D as seen in Fig.6 and Fig.7. However, the error relative to theoretical values, especially for C_L, is still significant. As expected, mesh D gives the best result as prism layers were used from the beginning.

Fig.8 shows the radius of the vortex core defined as the distance between the center of the vortex and maximum tangential velocity. Tangential velocity is computed by interpolating the velocity on circles of different radius and averaging along the tangential direction. From one mesh to another, the results are quite different. The sensitivity of the vortex core radius to the mesh for RANS calculations was already pointed out by Misaka in his work [10]. Kolomenskiy [5] explained that such behavior is likely due to truncation error. The effect of the mesh resolution can also be seen in Fig.9. Mesh convergence for the vortex radius seems to have been achieved for $\frac{x}{b} < 15$. It is interesting to observe that for mesh D and mesh B, the vortex core radius seems to vary linearly with the distance. Moreover, the radius is of the order of magnitude of the mean chord, which was already observed by Misaka [10] for LES simulations. Concerning mesh C, the vortex core radius is overestimated as the mesh of the vortex region is too coarse to accurately capture the tangential velocity profiles.

DOI: 10.13009/EUCASS2023-421

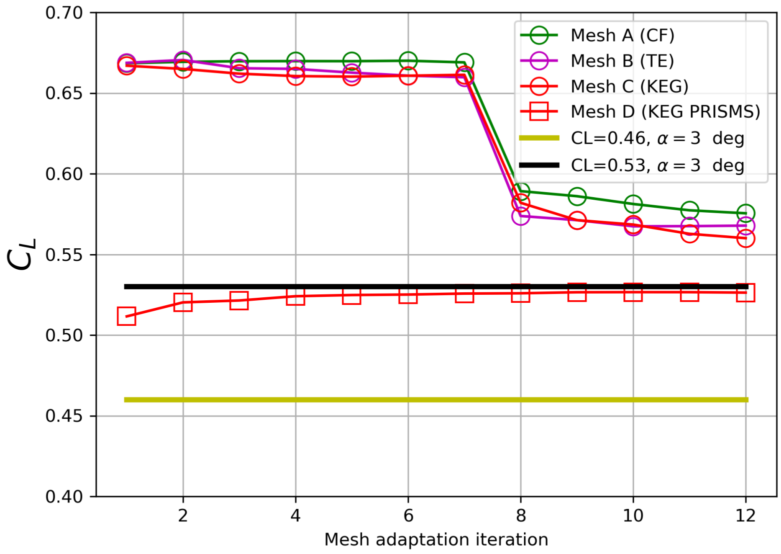

Figure 6: Lift coefficient C_L obtained in the simulations for the different sensors and mesh iterations. Experimental values are obtained from River's work [13].

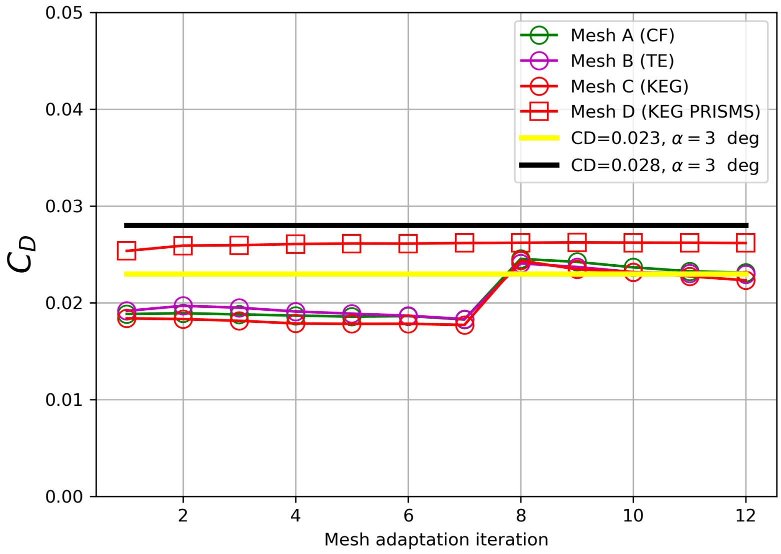

Figure 7: Drag coefficient C_D obtained in the simulations for the different sensors and mesh iterations. Experimental values are obtained from River's work [13].

4.2 Jet dynamic

In this section, we present the analysis of the simulation for the engine jet. Being able to accurately solve the jet region is important for contrail simulations in order to correctly resolve both chemistry and microphysics in that region. Fig.10 shows the static temperature field at the end of the domain, that is to say for $\frac{x}{b} = 20$. For mesh A, B and D, the roll-up of the jet around the wing-tip vortex can be observed which shows that the mesh is fine enough 1.2 km downstream of the aircraft to capture the underlying physics. For mesh C, no roll-up can be observed as the mesh is too coarse in that region and numerical diffusion killed both the jet and the wing-tip vortex. Some differences can be observed between mesh A, B and D. For mesh D, the jet appears more wrapped around the vortex compared to mesh A and mesh B. This

DOI: 10.13009/EUCASS2023-421

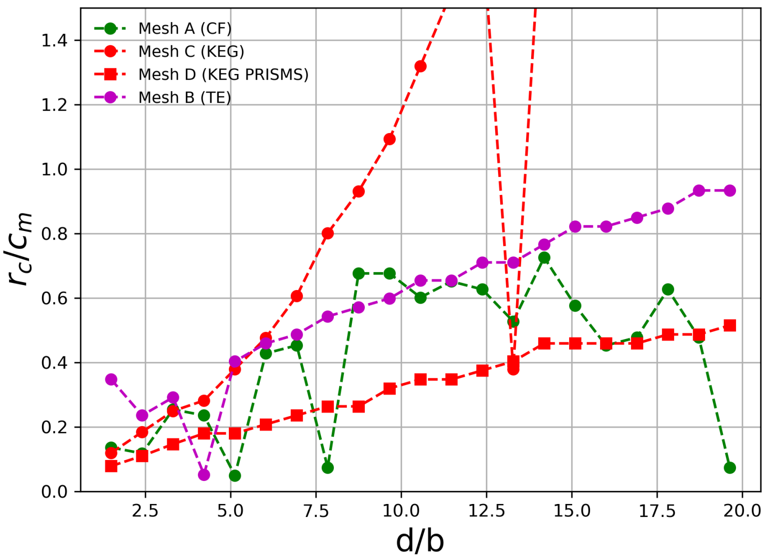

Figure 8: Radius of the vortex core r_c scaled by the mean chord c_m as a function of distance in wingspans for mesh iteration $n°12$

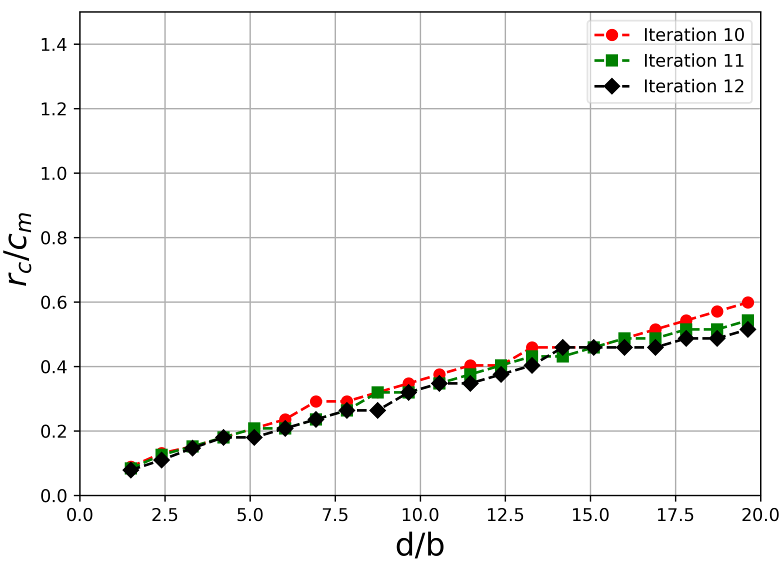

Figure 9: Radius of the vortex core r_c scaled by the mean chord c_m for mesh D as a function of distance in wingspans for mesh iteration $n°10$, 11 and 12.

DOI: 10.13009/EUCASS2023-421

can be explained by numerical diffusion of the momentum inside the vortex. The four meshes predict similar vortex circulation but different core radius which will result in different peak tangential velocities inside the vortex core. Mesh D presents the lowest radius as seen in Fig.8 and thus its maximum tangential velocity will be the highest among the four meshes. This will thus result in a higher wrapping of the jet around the vortex.

Fig.11 presents a slice on the y-axis of the mesh along with static pressure for the four different meshes. It can be observed that mesh D displays the finest mesh in the jet region while mesh A density is inferior. Those differences in the mesh can be observed for static pressure values. Indeed, for mesh C and mesh D, shock diamond structures in the jet region are more accurately resolved than in mesh A and mesh B. For mesh B, the size of the shock diamond structures is clearly smaller compared to the three other meshes. A close-up of the mesh in that region shows that the mesh is finer in the shock diamond region in mesh A, C and D compared to mesh B. However, the four meshes seem to correctly resolve the shock wave on the suction side of the wing even though the meshes are quite different in that region, especially for mesh A.

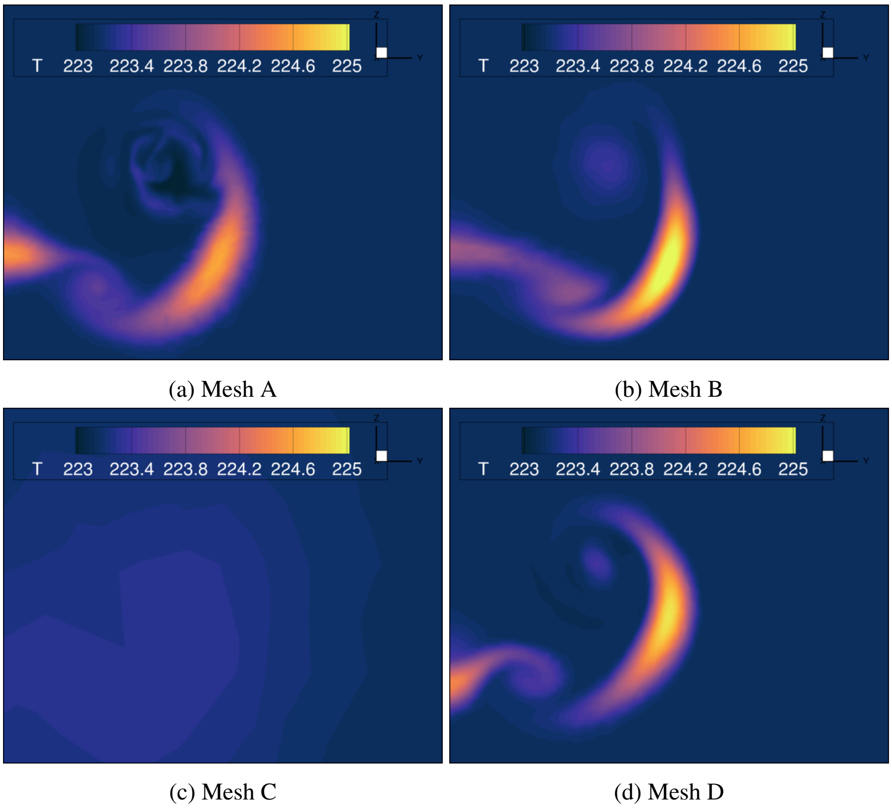

Figure 10: Static temperature field T [K] obtained on a cut along the x-axis for $\frac{x}{b}$ = 20 and for mesh iteration n°12

4.3 Temperature of the vortex core

An interesting finding of this work and potentially relevant for the study of contrails is the warming of the wing-tip vortex core. The static temperature field on a cut along the x-axis for $\frac{x}{b} = 1$ is plotted on Fig.12 for mesh D. It can be observed that static temperature is higher than ambient temperature in the vortex core and maximum at its center. The difference of temperature is about a few degrees. Such phenomenon was observed for all meshes (A, B, C and D) and gets more intense when the mesh is refined in the vortex core region. Colonius [3] studied theoretically the effects of compressibility on a 2D viscous Lamb-Oseen vortex and showed that for an initially homentropic vortex, static pressure and density decrease at different rates when distance to the vortex center decreases. This results eventually in an increase of static temperature inside the vortex core since temperature $T \propto \frac{p}{\rho}$ for an ideal gas. As Lamb-Oseen vortices are classically used to model wing-tip vortices, we can expect compressibility to have a very similar effect on wing-tip vortices.

DOI: 10.13009/EUCASS2023-421

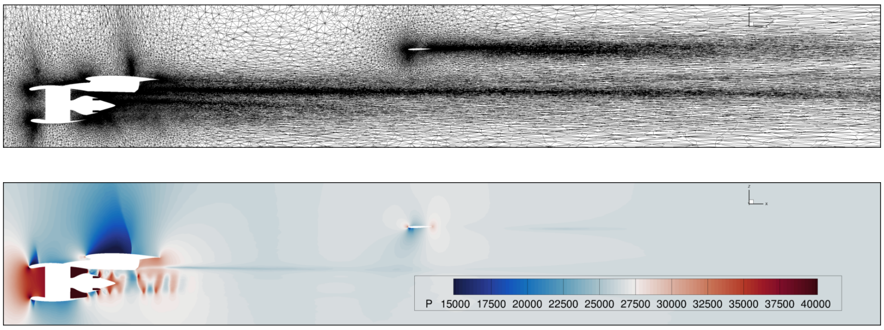

(a) Crossflow velocity sensor (mesh A)

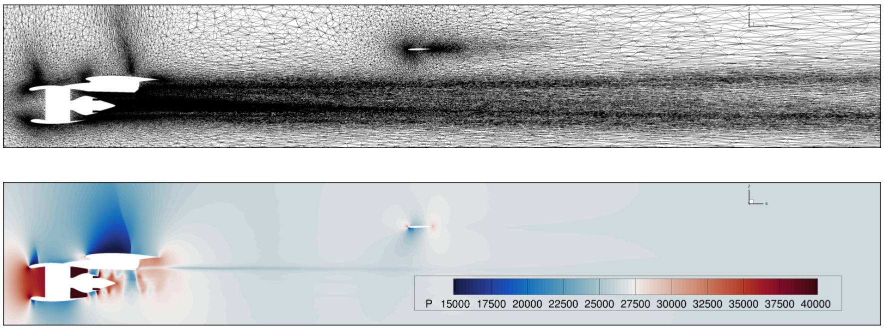

(b) Total energy sensor (mesh B)

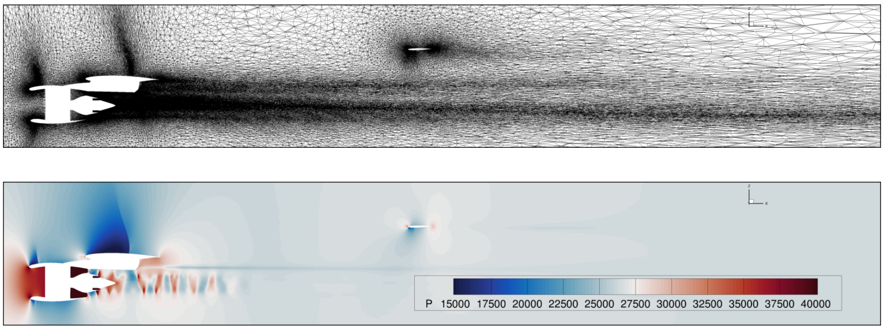

(c) Kinetic energy sensor (mesh C)

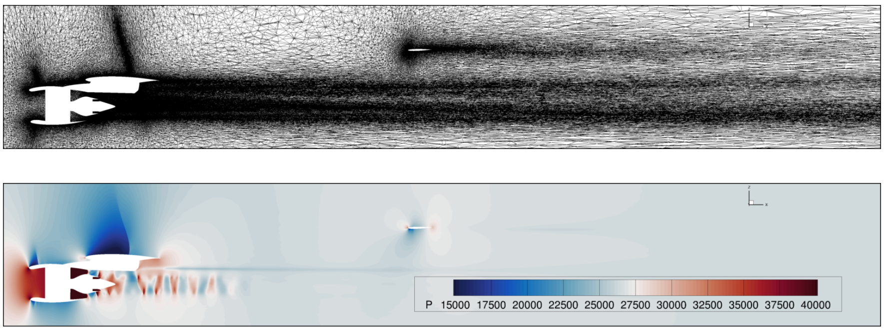

(d) Kinetic energy sensor with prisms (mesh D)

Figure 11: Mesh cut along the Y-axis and static pressure P [Pa] field of the jet region for mesh iteration $n°12$.

DOI: 10.13009/EUCASS2023-421

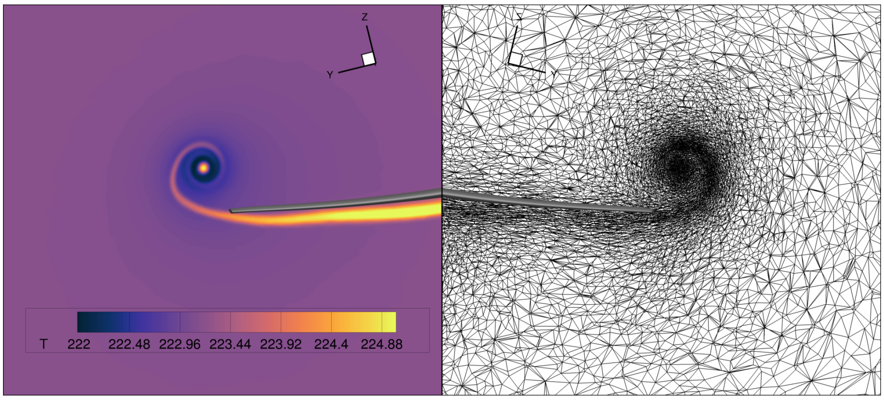

Figure 12: Cut along the x-axis for static temperature T [K] along with a mesh cut obtained one wingspan downstream of the aircraft. Mesh iteration $n°$ 12, mesh D.

5. Conclusion

In this paper, we have presented the results of CFD simulations of the near field of an aircraft during cruise flight using mesh adaptation techniques. The results demonstrate the effectiveness of mesh adaptation in improving the accuracy of the simulations by refining the mesh in areas of high gradient. Four different adaptation strategies were considered, based on different sensor variables and interpolation error norms. Mesh adaptation proved its ability to significantly improve vortex strength conservation throughout the domain for all meshes. Significant differences between the meshes arose for the flow field in the jet region. Those differences were mainly explained by the disparity in mesh resolution for the jet region with respect to the sensor variable used. Overall, the results of this work tend to show that using the kinetic energy sensor variable, along with L^2 norm and prism layers on the solid surfaces, is the best option to accurately resolve the flow physics in the near field of an aircraft. However, it is also the most expensive option, at least for the number of mesh iterations considered in this study. Future work will focus on enabling surface mesh adaptation on the solid surfaces and studying its effect on boundary layer mesh resolution.

6. Acknowledgment

The authors would like to express their gratitude to Direction Générale de l'Aviation Civile (DGAC) for providing the necessary funding to carry out this research.

References

[1] Frederic Alauzet and Loïc Frazza. 3d rans anisotropic mesh adaptation on the high-lift version of nasa's common research model (hl-crm). In *AIAA Aviation 2019 Forum*, page 2947, 2019.

[2] Aravind Balan, Michael A Park, William K Anderson, Dmitry S Kamenetskiy, Joshua A Krakos, Todd Michal, and Frédéric Alauzet. Verification of anisotropic mesh adaptation for turbulent simulations over onera m6 wing. *AIAA Journal*, 58(4):1550–1565, 2020.

[3] Tim Colonius, Sanjiva K Lele, and Parviz Moin. The free compressible viscous vortex. *Journal of Fluid Mechanics*, 230:45–73, 1991.

[4] Laurent Jacquin and Carlos Pantano. On the persistence of trailing vortices. *Journal of Fluid Mechanics*, 471:159–168, 2002.

[5] Dmitry Kolomenskiy and Roberto Paoli. Numerical simulation of the wake of an airliner. *Journal of Aircraft*, 55(4):1689–1699, 2018.

[6] David S Lee, David W Fahey, Agnieszka Skowron, Myles R Allen, Ulrike Burkhardt, Qi Chen, Sarah J Doherty, Sarah Freeman, Piers M Forster, Jan Fuglestvedt, et al. The contribution of global aviation to anthropogenic climate forcing for 2000 to 2018. *Atmospheric Environment*, 244:117834, 2021.

DOI: 10.13009/EUCASS2023-421

[7] Adrien Loseille and Frédéric Alauzet. Continuous mesh framework part i: well-posed continuous interpolation error. *SIAM Journal on Numerical Analysis*, 49(1):38–60, 2011.

[8] Adrien Loseille and Frédéric Alauzet. Continuous mesh framework part ii: validations and applications. *SIAM Journal on Numerical Analysis*, 49(1):61–86, 2011.

[9] Victorien Menier. *Numerical methods and mesh adaptation for reliable RANS simulations*. PhD thesis, Université Pierre et Marie Curie-Paris VI, 2015.

[10] Takashi Misaka, Frank Holzäpfel, and Thomas Gerz. Large-eddy simulation of aircraft wake evolution from roll-up until vortex decay. *AIAA journal*, 53(9):2646–2670, 2015.

[11] Emmanuel Montreuil, Weeded Ghedhaifi, Vivien Chmielaski, Francois Vuillot, Fabien Gand, and Adrien Loseille. Numerical simulation of contrail formation on the common research model wing/body/engine configuration. In *2018 Atmospheric and Space Environments Conference*, page 3189, 2018.

[12] Joris Picot. *Simulation aux grandes échelles de traînées de condensation dans un milieu atmosphérique stratifié et turbulent.* PhD thesis, Université de Toulouse III-Paul Sabatier, 2013.

[13] Melissa Rivers and Ashley Dittberner. Experimental investigations of the nasa common research model in the nasa langley national transonic facility and nasa ames 11-ft transonic wind tunnel. In *49th AIAA aerospace sciences meeting including the new horizons forum and aerospace exposition*, page 1126, 2011.

[14] Christopher L Rumsey, Jeffrey P Slotnick, and Anthony J Sclafani. Overview and summary of the third aiaa high lift prediction workshop. *Journal of Aircraft*, 56(2):621–644, 2019.

[15] Dieter Schwamborn and Mikhail Strelets. Ataac–an eu-project dedicated to hybrid rans/les methods. In *Progress in Hybrid RANS-LES Modelling: Papers Contributed to the 4th Symposium on Hybrid RANS-LES Methods, Beijing, China, September 2011*, pages 59–75. Springer, 2012.

[16] Simon Unterstrasser. Large-eddy simulation study of contrail microphysics and geometry during the vortex phase and consequences on contrail-to-cirrus transition. *Journal of Geophysical Research: Atmospheres*, 119(12):7537–7555, 2014.

[17] Simon Unterstrasser and Norman Görsch. Aircraft-type dependency of contrail evolution. *Journal of Geophysical Research: Atmospheres*, 119(24):14–015, 2014.